JOURNAL OF GEOPHYSICAL RESEARCH, VOL. 100, NO. A7, PAGES 12,201–12,215, JULY 1, 1995

Coherent radar estimates of average high-latitude ionospheric Joule heating

M. J. Kosch and E. Nielsen

Max-Planck-Institut für Aeronomie, Katlenburg-Lindau, Germany

Abstract. The Scandinavian Twin Auroral Radar Experiment (STARE) and Sweden and Britain Radar Experiment (SABRE) bistatic coherent radar systems have been employed to estimate the spatial and temporal variation of the ionospheric Joule heating in the combined geographic latitude range 63.8°–72.6° (corrected geomagnetic latitude 61.5°–69.3°) over Scandinavia. The 173 days of good observations with all four radars have been analyzed during the period 1982 to 1986 to estimate the average ionospheric electric field versus time and latitude. The *AE* dependent empirical model of ionospheric Pedersen conductivity by Spiro et al. (1982) has been used to calculate the Joule heating. The latitudinal and diurnal variation of Joule heating as well as the estimated mean hemispherical heating of 1.7×10^{11} W are in good agreement with earlier results. Average Joule heating was found to vary linearly with the *AE*, *AU*, and *AL* indices and as a second-order power law with *Kp*. The average Joule heating was also examined as a function of the direction and magnitude of the interplanetary magnetic field. It has been shown for the first time that the ionospheric electric field magnitude as well as the Joule heating increase with increasingly negative (southward) *Bz*.

Introduction

One of the major sinks of energy provided by the solar wind is ionospheric Joule heating caused by the dissipation of the Pedersen currents, the major part of the energy being deposited in the auroral zone. The pattern of these currents depends strongly on the interaction of the magnetosphere with the solar wind. In order to understand the energy budget associated with the coupling between the solar wind and the magnetosphere-ionosphere system, it is important to obtain good estimates of the Joule heating rate. Ionospheric Joule heating is the second most important energy sink after the ring current [*Akasofu*, 1981] and generally amounts to several times that associated directly with particle precipitation [e.g., *Banks et al.*, 1981; *Ahn et al.*, 1983], but the latter may also sometimes be the most important [*Harel et al.*, 1981]. Auroral particle precipitation, although a determining factor for ionospheric conductivity, is generally less important as a supply of energy to the ionosphere [*Cole*, 1975; *Akasofu*, 1981].

Calculation of the Joule heating density involves the product of the Pedersen conductivity and the square of the electric field ($Q(j) = \mathbf{P} \times \mathbf{E}^2$ W/m^2). The total ionospheric electric field consists of the electrostatic field plus the neutral wind (U), giving E(total) = E(static) + ($\mathbf{U} \times \mathbf{B}$). To obtain the total power dissipated in the area swept out by the radars during 24 hours, the Joule heating density must be integrated over the total area covered. Unfortunately, Joule heating is very difficult to monitor continuously over the entire polar region. Generally, simultaneous observations of ionospheric conductivities and electric fields are confined to point measurements or to latitudinal profiles. Direct measurements of these quantities with rocket-borne experiments [e.g., *Evans et al.*, 1977; *Theile et al.*, 1981] or with incoherent radars such as Chatanika and European Incoherent Scatter (EISCAT) [e.g., *Wickwar et al.*, 1975; *Brekke*, 1976; *Banks et al.*, 1981; *Vickrey et al.*, 1982; *Brekke et al.*, 1991] can only provide Joule heating estimates over a small area. Therefore geomagnetic indices such as *Kp*, *AE*, or *AL* have been employed in the past as an approximate measure of the average global ionospheric Joule heating [e.g., *Ahn et al.*, 1983; *Foster et al.*, 1983; *Baumjohann and Kamide*, 1984], since they are readily available. Unfortunately, these studies generally tended to be based on relatively small data sets.

The Scandinavian Twin Auroral Radar Experiment (STARE) [*Greenwald et al.*, 1978] and Sweden and Britain Radar Experiment (SABRE) [*Nielsen et al.*, 1983] coherent radar systems have proven to be valuable tools for geophysical research in the high-latitude *E* region. Both STARE and SABRE use two identical VHF crossed-beam radars, which are located in Norway and Finland and in Britain and Sweden, respectively. The auroral radars are sensitive to electrostatic plasma waves [*Fejer and Kelley*, 1980] at about 105-km altitude, which are excited when the threshold ionospheric electric field of about 15 mV/m is exceeded [*Cahill et al.*, 1978]. The mean Doppler shift of the frequency of the transmitted radar signal is closely related to the phase velocity of these waves. Simple fluid theory predicts that the electrostatic plasma wave phase velocity in a given direction should be equal to the component of the electron drift velocity in that direction. Since electrons are known to be generally $\mathbf{E} \times \mathbf{B}$ drifting at *E* region altitudes, the electric field vector may be simply computed. Thus both systems provide good estimates of the horizontal electric field vector over a large field of view (5° latitude × 13° longitude) with high spatial resolution (0.2° latitude × 0.5° longitude) and good temporal resolution (typically 20 s). Figure 1 illustrates

Paper number 95JA00821.
0148-0227/95/95JA-00821$05.00

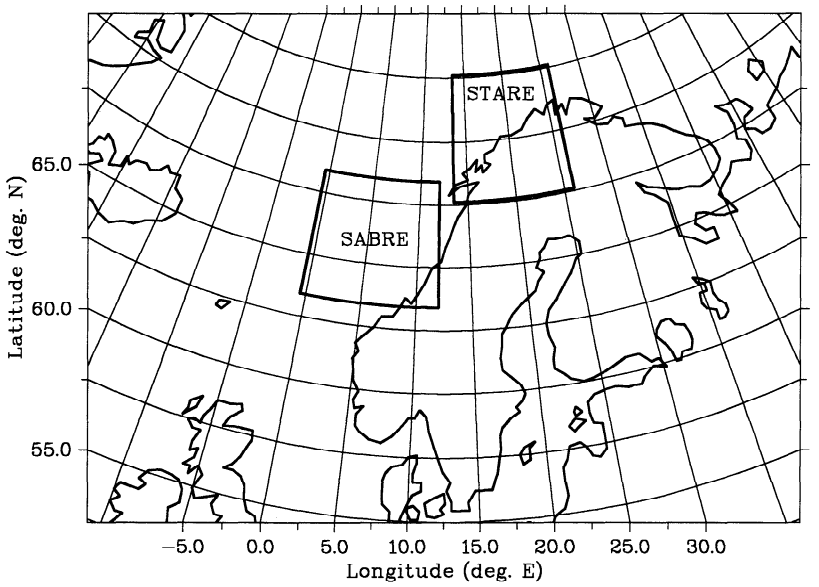

Figure 1. Geographic fields of view of the STARE and SABRE radars.

the geographic coverage offered by the two radar systems. STARE covers a geographic area of 67.6°–72.6°N and 13.5°–26.0°E, while SABRE covers 63.4°–68.4°N and 0.5°W–12.5°E. The combined corrected geomagnetic latitudinal coverage is approximately 61.1°–69.3°. Since ionospheric Joule heating predominates in the magnetic latitudes 60°–80° [*Ahn et al.*, 1983], we cover the lower half of this band with high time and spatial resolution. On average, for STARE, MLT = UT + 2.5 hours, and for SABRE, MLT = UT + 1.5 hours.

Unfortunately, the real-time distributions of the height-integrated ionospheric Pedersen conductivities are generally not available. However, the average distributions of this quantity are available in the literature for the entire polar region. Since our study is of a statistical average nature over a large data set, an averaged empirical model is necessary and sufficient. Both *Wallis and Budzinski* [1981] and *Spiro et al.* [1982] have produced empirical models of high-latitude ionospheric conductivity distributions in convenient tabular form. *Hardy et al.* [1987] have produced functional fits of the same. All the models use satellite particle data averaged over many months, hence smoothing out substorm and seasonal variations. The model of Wallis and Buzinski was produced for two ranges of Kp ($Kp \leqq 3$, $Kp > 3$) with 2° latitude and 2-hour time steps, while that of Spiro et al. included four ranges of the hourly averaged AE index ($AE < 100$, $100 < AE < 300$, $300 < AE < 600$, $AE > 600$ nT) with 1° latitude and hourly time steps. The functional model of Hardy et al. was produced for integral Kp steps from 0 to 5 and $Kp \geqq 6-$. Both *Spiro et al.* [1982] and *Vickrey et al.* [1981] have pointed out computation errors with Wallis and Budzinki's model. *Hardy et al.* [1987] found that his functional fits agreed approximately with Wallis and Buzinski but differed significantly from Spiro et al., although the reason for this was unclear. *Schlegel* [1988] has derived E region conductivities from EISCAT radar data and found that both Wallis and Budzinski and Spiro et al. predicted significantly higher conductivity values and that there were also diurnal discrepancies. He suggested that, for satellite data, uncertainties in the solar UV contributions to conductivity might be responsible. *Ahn et al.* [1989] also found that the Spiro et al. conductance model generally gave an overestimate but stated that the globally integrated heating rates are not very sensitive to the choice of conductance model (about 10% variation). It is clear that none of the statistical conductance models are suitable for studying individual events and that each one will result in a slightly different Joule heating distribution, even with averaging.

For this study, we have chosen to use the model of *Spiro et al.* [1982], it being the most detailed of the available models in tabular form. Figure 2 illustrates the Pedersen conductivity model in our latitude range of interest, Figures 2*a*–2*d* corresponding to the different AE ranges. In all cases, the Pedersen conductivity increases with magnetic latitude, and there is a noticeable diurnal variation, with the minimum and maximum occurring around magnetic midday and midnight, respectively. The diurnal variation increases strongly with increasing AE index.

Brekke et al. [1974] found, using Chatanika radar data, that the neutral wind is of considerable importance during quiet days in the auroral zone and may oppose the current driven by the electric field. *Heppner and Miller* [1982], using chemical release rockets, have shown that the neutral wind speed at about 105 km, although usually highly variable, can generally be expected to be less than 100 m/s. E region neutral wind speeds obtained using the Chatanika incoherent radar [*Brekke et al.*, 1973] support this expectation. This value (100 m/s) is well below the radars' threshold (15 mV/m $\geqq$ 300 m/s) and will produce a significantly smaller error than that posed by the radars' thresholding (discussed below), given the quadratic relationship of Joule heating upon an electric field. For example, a neutral wind of 100 m/s would correspond to an electric field of about 5 mV/m in our latitude range, and assuming a conductivity of 10 mho, this corresponds to a Joule heating rate of only 0.25 mW/m^2. For the same conductivity, the radars' threshold corresponds to a Joule heating rate of 2.25 mW/m^2. Hence for our analysis,

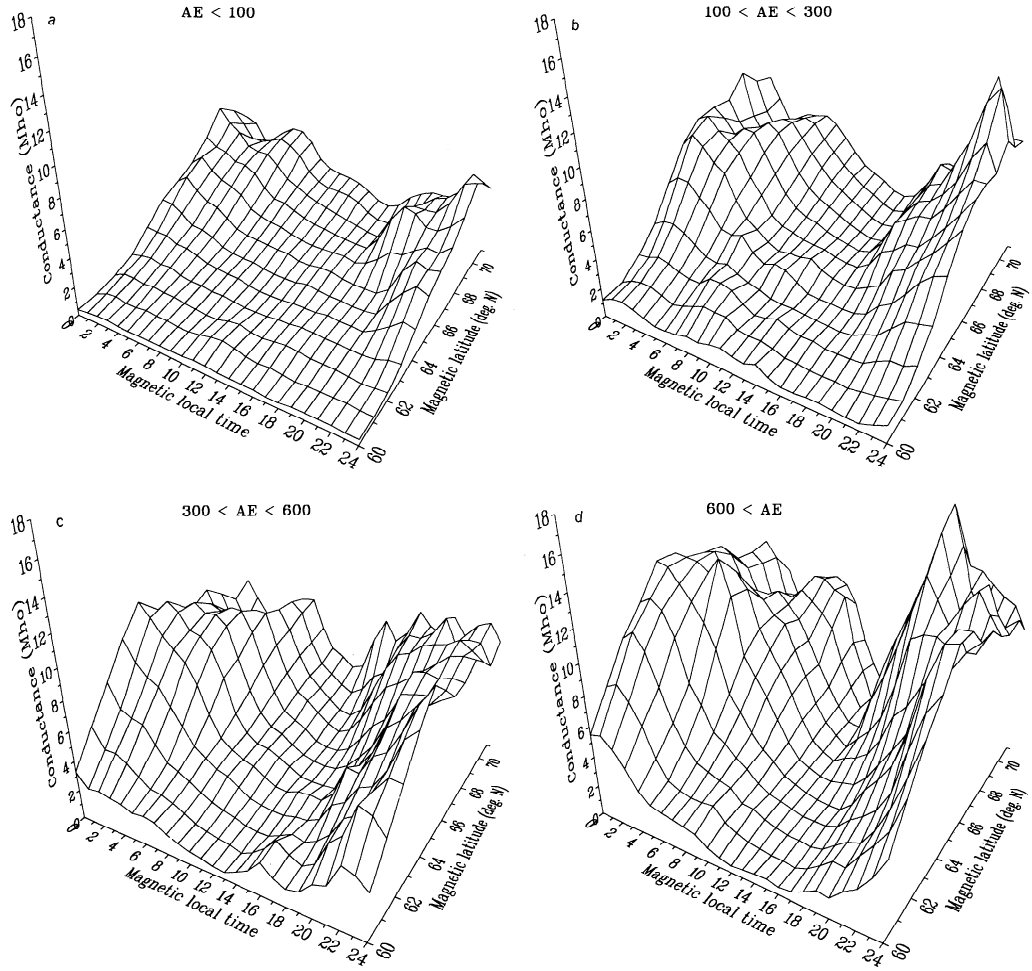

Figure 2. Pedersen conductivity model of *Spiro et al.* [1982] for (a) $AE < 100$, (b) $100 < AE < 300$, (c) $300 < AE < 600$, and (d) $AE > 600$ nT.

the effect of any neutral winds can safely be ignored, as will also be seen below.

We have combined data from the STARE and SABRE coherent radars in order to get estimates of the average E region ionospheric electric field in the geographic latitude range 63.8°–72.6° (corrected geomagnetic latitude 61.5°–69.3°) for all local times and a wide range of geophysical conditions. The AE-dependent empirical model of height-integrated Pederson conductivity by *Spiro et al.* [1982] was employed to calculate the ionospheric Joule heating rate as a function latitude and time. *Ahn et al.* [1983] found that the geomagnetic indices AE and, particularly, AL make good indicators of the global energy deposition rates. To test this and other indices, the Joule heating has been computed as functions of the Kp, AE, AU, and AL indices as well as the interplanetary magnetic field components. The empirical functional relationships are then determined by curve fitting.

Data Analysis

In order to use the STARE and SABRE radar data for estimating the ionospheric electric fields correctly, certain characteristics must be understood. As previously stated, the radars have a threshold of about 15 mV/m [*Cahill et al.*, 1978], below which no backscatter is generally received. This corresponds to an electron flow velocity of 300 m/s. Due to the large field of view of both radar systems, the aspect angle of the radar beams with respect to the magnetic field varies. *Nielsen* [1986] has experimentally determined the relationship between plasma wave phase velocity and aspect angle for the STARE radar, and we use this to normalize the electron flow vectors to 90° aspect angle over both radars' field of view. Comparisons between STARE and EISCAT electron drift velocities have been performed by *Nielsen and Schlegel* [1983, 1985]. They found that the magnitudes of the electron drift velocities were in good agreement for small velocities up to 700 m/s (35 mV/m) but that STARE increasingly underestimates the velocity magnitude for greater flow speeds. This is attributed to limiting of the plasma waves to the local ion acoustic velocity [*Kofman and Nielsen*, 1990]. The directions of the estimated vectors, however, are in good agreement for all drift magnitudes. Nielsen and Schlegel have developed an empirical algorithm for correcting the STARE magnitudes, which we use for the electric field vector estimate. Unfortunately, this comparison was logistically impossible to perform with SABRE, but is nevertheless used, since SABRE is functionally identical to STARE. Although it is realized that employing these corrections will increase the uncertainty of the electric field estimate for a single measurement, the averag-

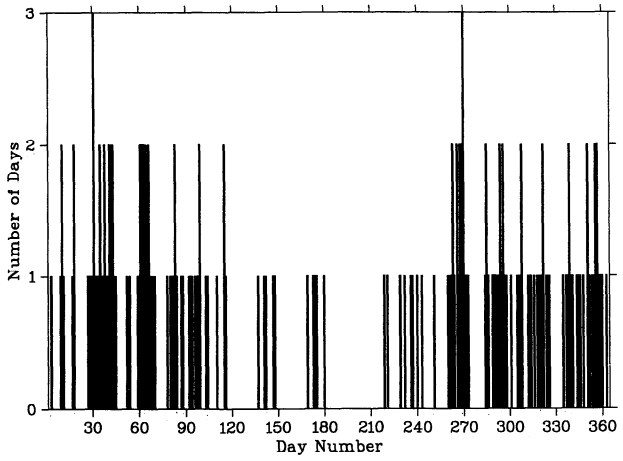

Figure 3. Annual distribution of data for selected days.

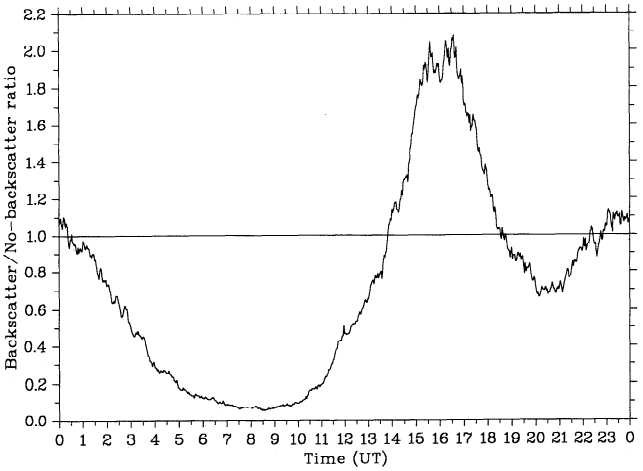

Figure 4b. Diurnal variation of the average backscatter/no-backscatter ratio.

ing we employ over a large data set will greatly reduce these statistical variations.

For the period 1982–1986, the entire data set was scanned for 24-hour periods for which all four stations were operating for most of the day. Data selection then proceeded subjectively based on the only requirement that the amount of backscatter occurrence in space and time should be maximized. This is important, since there are many intervals for which no backscatter is observed at any latitude because the ionospheric electric field strength is below the threshold of 15 mV/m. Even so, of the 173 periods of 24 hours selected, approximately half of the data fall into this category, although this ratio is strongly time dependent. As will be seen below, thresholding does not seriously affect the result, as Joule heating is proportional to the square of the electric field. Figure 3 shows the annual distribution of 24-hour periods for our data set. Of the 173 days analyzed, 57 occurred during winter (November–January), 10 during summer (May–July), and the remaining 106 during the equinoxes. This distribution is consistent with the annual variation we routinely observe in the backscatter data. Two thirds of the data come from the years 1983 and 1984, when all four radars were functioning very well.

Figure 4a shows the distribution of our data set against time and Kp for whenever either radar system received backscatter. Clearly, most of the data occur for $3 \leqq Kp \leqq 5$. The lack of data for $Kp < 2$ is due, in part, to the radars' threshold and is consistent with the finding of *Zi and Nielsen* [1982]. There is a noticeable reduction of data centered around 0730 UT (late magnetic morning), and higher Kp values are required here for the radar to receive backscatter. *Waldock et al.* [1985] found a similar distribution using backscatter intensities from the SABRE radar only. Figure 4b shows the diurnal variation of average backscatter to no-backscatter ratio integrated over all latitudes. Clearly, the amount of backscatter observed is highly time dependent. In the time zone 0400–1300 UT, relatively little backscatter is received at any latitude on average. The peak centered around 1600 UT corresponds to the eastward electrojet (about 1300–1800 UT), where up to two thirds of the data exceed the radars' threshold. During the westward

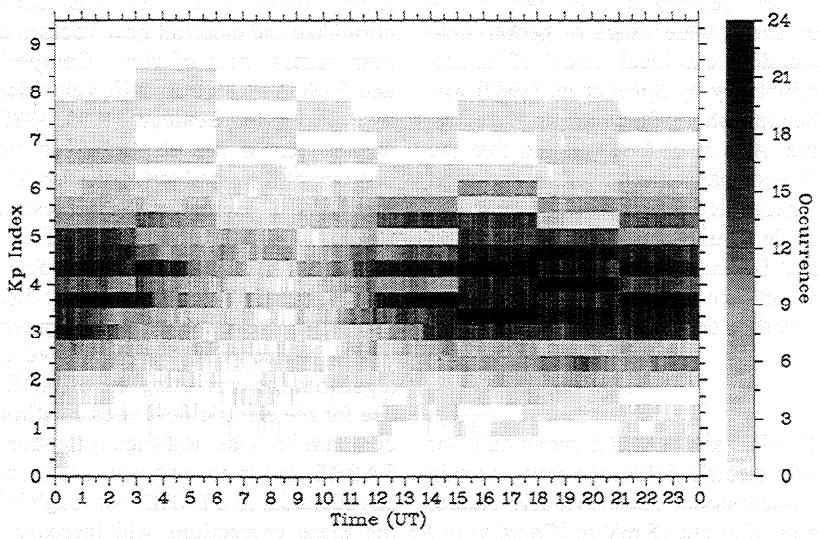

Figure 4a. Data distribution versus time and Kp.

electrojet (about 2100–0004 UT), significantly less backscatter is received, about one half to one quarter of the data exceeding the threshold. At this time, the STARE radar generally receives more backscatter than the SABRE radar. Clearly, Figures 4a and 4b complement each other.

For both radar systems, a latitudinal profile of electron flow vectors through the center of their fields of view was extracted every 20 s. Each such profile is made up by averaging over 2.5° of longitude, and so a running average is performed through time. These vectors are then subject to the aspect and empirical corrections described earlier. In order to reduce the data volume to a manageable size, these data are then binned into 2-min averages, giving 720 data points through time per day. The maximum resolution of 0.2° is retained through latitude. The magnetic field strength is approximately 0.5 G within both radars' fields of view, and assuming that the electrons in the E region are $\mathbf{E} \times \mathbf{B}$ drifting, the electron flow vector is converted into the equivalent electric field vector simply by rotating clockwise through 90° and using the relationship 1000 m/s ↔ 50 mV/m. Knowing the MLT for each radar system and the hourly average AE index value, *Spiro et al.*'s [1982] conductivity model is then employed to calculate the Joule heating density for each 2-min interval and latitude point. Although the conductivity model is interpolated for each latitude and time, only the hourly average AE values are used to determine which of the four model ranges is to be used throughout that hour. As has been stated earlier, the effect of neutral winds is ignored. Since a significant fraction of the data fall below the radars' threshold (see Figure 4b), it is important in the averaging process and must be considered. These data are routinely set equal to 7.5 mV/m, since we know that such data must lie between zero and 15 mV/m. Of course, the vector directions of these data are unknown.

Since it takes one complete day to scan all local times, we are unable to generate an instantaneous picture of the hemispherical Joule heating. To produce the statistical average Joule heating within our latitude range, averaging over all the 173 selected days is required in order to remove localized fluctuations such as substorm effects. The data sets from both radar systems are combined, averaging together in the region of overlap, to give a geographic latitudinal field of view of 63.8°–72.6° (corrected geomagnetic latitude 61.5°–69.3°). The two lowest ranges of SABRE rarely received any signal, probably due to poor aspect angle, and hence have not been included in the analysis.

Results and Discussion

The diurnal variation of the average instantaneous power averaged over the combined field of view for the entire data set is shown in Figure 5a. The diurnal variation consists of two broad peaks, the larger and smaller ones occurring around 2100–0004 and 1300–1800 UT, respectively. There is a marked reduction of heating around 0500–1200 UT, with the energy dissipated dropping by almost an order of magnitude in the interval 0300–0500 UT. Figures 5b and 5c show similar plots but for westward and eastward electrojet region data only, respectively. For the westward (eastward) electrojet region, any equatorward (poleward) pointing electric field vector within ±45° of magnetic south (north) has been included in the data analysis. Any electric field vector with another direction is simply ignored. In these two cases, the

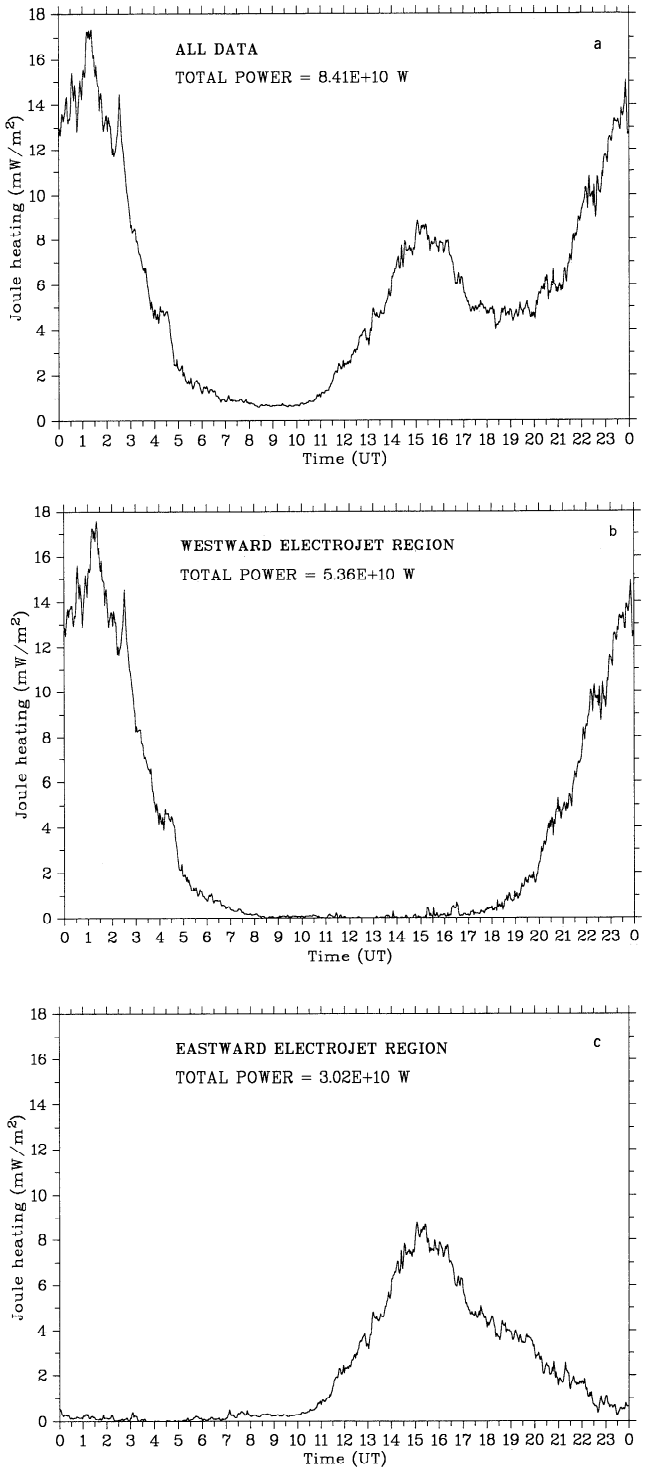

Figure 5. Average diurnal variation of Joule heating for (a) all data, (b) westward electrojet region only, and (c) eastward electrojet only region.

electric field strength was set to zero when no backscatter was received, as the vector direction for these data was unknown. Figures 5b and 5c clearly illustrate that the diurnal variation illustrated in Figure 5a is dominated by the combined contributions from the eastward and westward electrojet regions. The total power dissipated is obtained by integrating over the common area scanned by both radar systems (1.49×10^{13} m^2), giving 3.02×10^{10} W and $5.36 \times$

10^{10} W for the eastward and westward electrojet regions, respectively, and 8.41×10^{10} W for the total area. The westward electrojet region dissipates almost 80% more energy than the eastward electrojet region, and the sum of the two accounts for over 99% of the total power dissipated. The reason for so little power dissipation outside of the electrojet regions is that low electric field strengths are generally observed within the radars' latitude range at these times. Figure 4b illustrates that many more than half the observations fall below the radars' threshold of 15 mV/m for these times.

Plate 1 shows the average instantaneous Joule heating density versus latitude and time for the entire combined data set. The nonlinear color scale gives the heating density in units of mW/m^2. Since the data are collected using geographic UT coordinates, we have found this the most natural way to plot the data. The figure is orientated such that magnetic midnight and midday are approximately located at the bottom and the top of the diagram, respectively. For STARE, MLT = UT + 2.5, and for SABRE, MLT = UT + 1.5 hours. Obviously, Figure 5a and Plate 1 are based on identical data. With reference to Figures 5b and 5c, the westward and eastward electrojet regions are clearly seen in Plate 1 before and after magnetic midnight, respectively, as regions of enhanced heating. Clearly, more energy is dissipated over a larger latitude range and time zone in the westward than the eastward electrojet region. Although the average Joule heating density only exceeds 20 mW/m^2 at the peaks, on individual days it is not uncommon for this value to exceed 50 mW/m^2 in localized areas.

The Harang discontinuity shows itself in Plate 1 as a region of reduced heating around 1800–2000 UT. *Banks* [1977], using the Chatanika radar, and *Kamide et al.* [1986], using satellite optical and magnetometer data, also found a pronounced decrease in Joule heating in the midnight sector of several hours' duration. *Banks* [1977] attributed this to the smaller electric fields of the Harang discontinuity. *Banks et al.* [1981], using the Chatanika radar, and *Ahn et al.* [1983], using satellite X ray and magnetometer data, showed that strong localized heating can occur around magnetic midnight on occasion. In the averaging procedure we employ, however, such occasional and localized heating would not play a significant role. During the magnetic midday hours (0600–1200 UT) there is a broad region of very low heating (<1 mW/m^2), especially at lower latitudes. *Foster et al.* [1983], using averaged satellite data, found that the most intense Joule heating regions tended to occur in the day sector, where solar-produced conductivities are high, but is confined to a spatially small region. *Banks et al.* [1981] and *Ahn et al.* [1989], using Chatanika radar and magnetometer data, respectively, produced similar results on occasion. We do not observe this feature, this being due to the generally low electric field strengths as indicated by the lack of backscatter during the same time interval (see Figure 4). Since this region only receives backscatter during high Kp, intense heating may occur on occasion, but the average remains low.

Several attempts have been made to produce either instantaneous, daily, or averaged patterns of global hemispherical Joule heating by a variety of methods [e.g., *Banks et al.*, 1981; *Vickery et al.*, 1982; *Foster et al.*, 1983; *Ahn et al.*, 1983, 1989; *Kamide et al.*, 1986]. The pattern of average hemispherical Joule heating shown in Plate 1 coincides well with those produced by others. Discrepancies do exist, but these may be attributed to either their very small data sets or possibly the entirely different experimental technique.

We have experienced difficulties in matching the STARE and SABRE data smoothly together. The matching is much better when plotted in geographic UT as opposed to geomagnetic MLT coordinates. When combined into geomagnetic MLT coordinates, we find that substantial discontinuities occur between the STARE and SABRE data. This is partly due to the fact that SABRE generally appears to receive less backscatter than STARE, even for the same geomagnetic conditions in the overlapping latitude band. The reason for this probably is that the SABRE radars have a less favorable aspect angle to the magnetic field lines when compared with STARE, especially in the overlap region. This may indicate a higher backscatter threshold for SABRE. Upon trying different magnetic field mapping algorithms, it was not very surprising to find small disagreements. We have also found that the matching of the data is sensitive to changes in conductivity as a result of using different magnetic field models giving some variation in latitude.

In order to deconvolve the combined effects of ionospheric conductivity and electric field variations, we have simply repeated the entire Joule heating computation using a constant uniform conductivity value instead of *Spiro et al.*'s [1982] empirical conductivity model. This procedure effectively illustrates the electric field squared variations. Plate 2 shows the result using exactly the same scale and format as for Plate 1. In order to facilitate comparison, the conductivity has been set to 5.85 mhos, so that the total power for both Plates 1 and 2 is approximately equal. With reference to Figures 5b and 5c, the westward and eastward electrojet regions are clearly seen in Plate 2 before and after magnetic midnight, respectively, as regions of enhanced heating. More energy is dissipated in the eastward than the westward electrojet region, which is the reverse of that illustrated in Plate 1. When compared with Plate 1, the eastward electrojet region is expanded toward lower latitudes, while that of the westward electrojet region is reduced in intensity. The Harang discontinuity shows itself as a region of reduced heating around 1800–2200 UT. Clearly, the most obvious effect of *Spiro et al.*'s [1982] conductivity model is to make postmagnetic midnight a region of greater energy dissipation when compared with premagnetic midnight, even though the electric field strength appears to be greater over a larger time and latitude region before magnetic midnight than after magnetic midnight.

Integrating over the entire area covered by both radar systems in 1 day (1.49×10^{13} m^2) gives the total power dissipated in the ionosphere. For the case shown in Plate 1, where the electric field strength has been set to 7.5 mV/m whenever no backscatter is received, the total power is $Q(j) = 8.42 \times 10^{10}$ W. In order to check the effects of radar thresholding, the total power has been computed for the electric field strength set to zero and 15 mV/m whenever no backscatter is received, giving 8.17×10^{10} and 9.18×10^{10} W, respectively. It is clear that the uncertainty resulting from the radars' threshold is less than 10% and that using 7.5 mV/m in these cases is reasonable. From Figure 4b, it is clear that uncertainty introduced by thresholding is highly time dependent. During the electrojets, where a high proportion of backscatter is received, the uncertainty will be low, especially bearing in mind that Joule heating is proportional to the electric field squared. It is during the magnetic midday

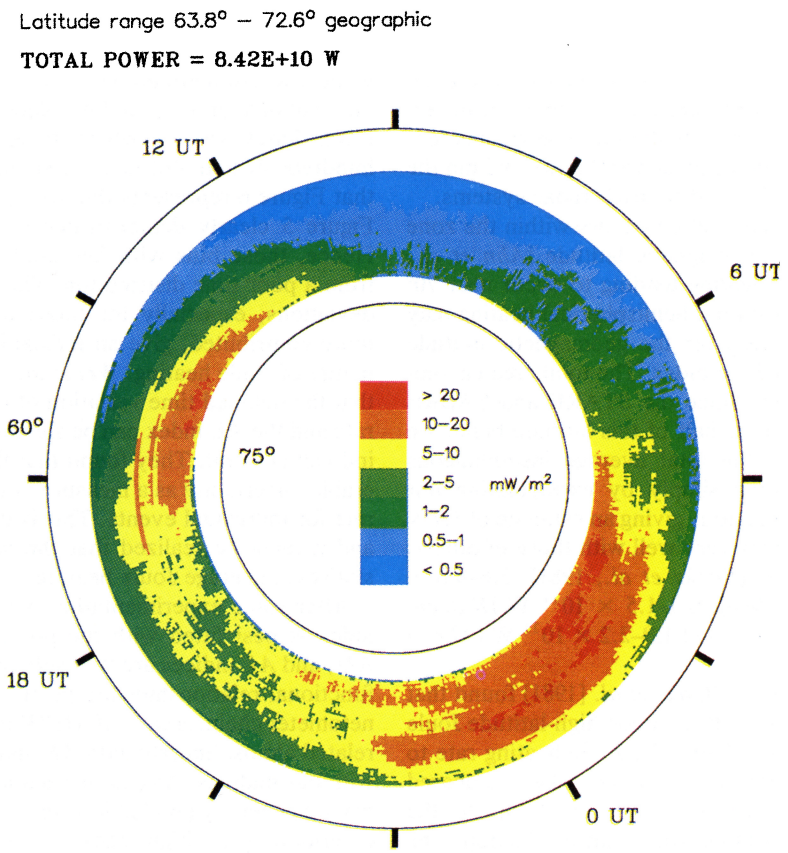

Plate 1. Average ionospheric Joule heating using the empirical conductivity model of *Spiro et al.* [1982].

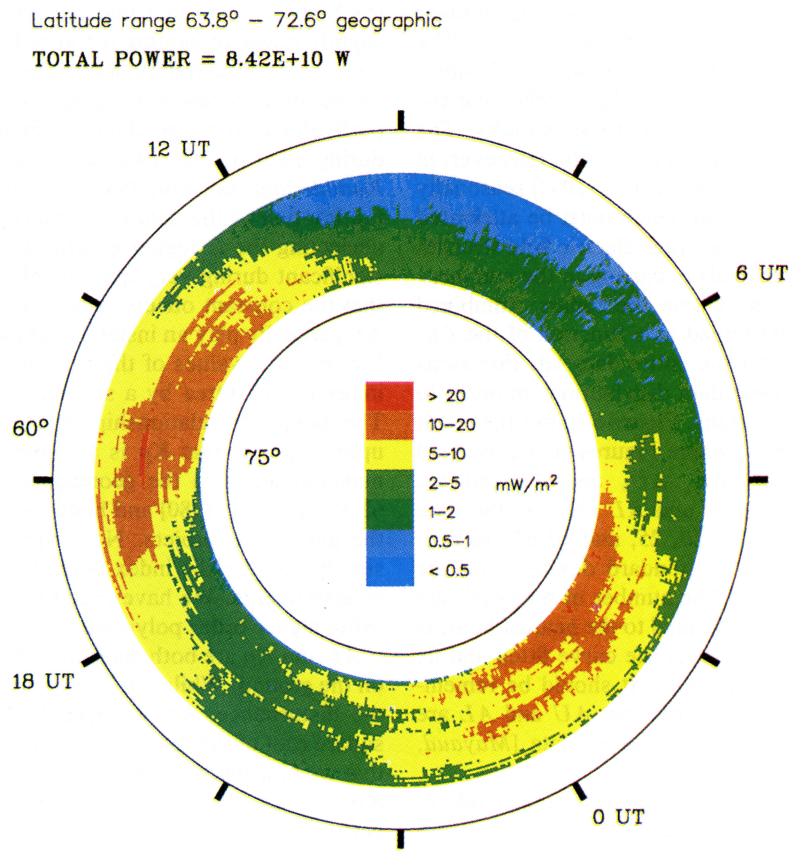

Plate 2. Average ionospheric Joule heating using a constant uniform conductivity of 5.85 mhos.

hours where very little backscatter is received (see also Plate 1) that radar thresholding will introduce a significant uncertainty. Fortunately, this period of the day contributes less than 5% to the total average hemispherical power within the fields of view of the STARE and SABRE radar systems.

Most of the Joule heat dissipation occurs within the zone bounded by 60° and 80° geomagnetic latitude [*Ahn et al.*, 1983], with the strongest heating tending to occur near 70° [*Banks et al.*, 1981]. Hence total hemispherical heating may be estimated by integrating over the geomagnetic latitude range 60°–80° and over all longitudes. The total area encompassed is 3.03×10^{13} m^2. Since the STARE and SABRE radar systems scan the lower half of this latitude band, we can get a rough idea of the total average instantaneous hemispherical Joule heating simply by extrapolating our measured result shown in Plate 1, giving an estimate of 1.7×10^{11} W. Our estimate agrees very well with those of others, for example, 10^{11}–10^{12} W [*Banks et al.*, 1981], 5.6–8.8 $\times 10^{11}$ W [*Kamide et al.*, 1986], 0.3–1.5 $\times 10^{11}$ W [*Killeen*, 1987, and references therein], and 1.9–2.2 $\times 10^{11}$ W [*Ahn et al.*, 1989].

Using the Chatanika radar, *Banks et al.* [1981] found that there are significant seasonal effects upon high-latitude Joule heating. *Foster et al.* [1983] found the Joule heating rate to be 50% greater in the summer hemisphere when compared with the winter hemisphere. They attributed this to the increased conductivity resulting from solar production. The total average power within the radars' combined field of view has been computed for the summer (May–July), winter (November–January) and equinox months, giving 1.18×10^{11}, 6.93×10^{10}, and 8.88×10^{10} W, respectively (not illustrated). Bearing in mind the increased uncertainty associated with the lack of summer data (10 days), the summer average exceeds that for the winter by about 70%. The equinox average lies between those for summer and winter and is close to the total average in Plate 1, reflecting the preponderance of data (106 days) for these months. The seasonal trend is well supported by our results. However, in our case it cannot come from *Spiro et al.*'s [1982] seasonally averaged conductivity model and hence must be attributed to a small seasonal variation of average electric field strength (about 8%), with the larger fields occurring in the summer.

The average Joule heating within the radars' combined field of view has been determined as a function of the *Kp*, *AE*, *AU*, and *AL* indices for the entire data set. Functions have then been fitted to these data distributions in order to get convenient empirical relations. Figure 6 shows the result of this process as bar graphs, where Figures 6a, 6b, 6c, and 6d correspond to the *Kp*, *AE*, *AU*, and *AL* indices, respectively. For the *AE*, *AU*, and *AL* indices, the data have been binned into steps of 50, 25, and 50 nT, respectively. For each bin, twice the standard deviation on the mean is plotted as a solid bar. The number of hours of data contributing to each average, rounded to the nearest hour, is given above each bin. In each case, the curve fitted and its equation are also given in the figure. It should be remembered that $AE = AU - AL$ nT and that *AU* and *AL* are extracted from the identical magnetometer data [*Mayaud*, 1980].

Clearly, in all cases, the average Joule heating tends to increase with increasing index value. However, there are some exceptions, for example, $Kp = 7$ and 7+ or $AE = 1000$ nT. These exceptions only occur at higher index values, where there are relatively few contributions (tens of hours of data or less), and we place a far greater store on the lower index values, where there are contributions from hundreds of hours of data. It should also be borne in mind that Figure 6 represents the average Joule heating, whereas Figure 5 clearly demonstrates a strong diurnal variation. Hence, those bins with few contributions may also suffer from a poor time distribution. The relatively large standard deviations, especially for those bins where 100 hours or more contributed, give an indication of the highly variable nature of Joule heating. *Wei et al.* [1985] have demonstrated that the detailed time variation of the Joule heat production rate and the *AE* index can be significantly different during an individual event. They found that the *AE* index had considerable uncertainty as a measure of the Joule heat production rate for individual events. This is borne out in our analysis, and it must be realized that the indices can only give the statistical average Joule heating.

After some experimentation, we have found that the *Kp* index is best fitted with the power law, whereas the *AE*, *AU*, and *AL* indices are well served by linear functions. The functional relationships are given in Table 1. Using a magnetometer chain, *Ahn et al.* [1983] found that Joule heating is related almost linearly with *AE* and *AL*, which is consistent with our findings. As can be seen in Figure 6, the functional fits are generally good at low and middle range index values, deteriorating for high index values due to the lack of data. The linear fit is consistent with the fact that the 12 primary magnetometers contributing to these indices lie in the geomagnetic latitude range 60.04°–71.21° [*World Data Center C2 for Geomagnetism*, 1993], which is only slightly greater than the combined coverage of the STARE and SABRE radars (61.1°–69.5°). The fact that the *AE* and *AL* indices predict slightly negative heating for very low values may be partly due to the uncertainty associated with the lack of radar backscatter during very quiet conditions (see Figure 4), partly due to the rapid decrease in accuracy of these indices during quiet periods ($AE < 250$ nT) [*Akasofu et al.*, 1983; *Kamide and Akasofu*, 1983], which accounts for a substantial fraction of the data (see Figure 6), and partly due to us neglecting the *E* region neutral winds, which may become significant during very quiet conditions. It should be noted that the constant offsets in the equations for *AE*, *AU*, and *AL* generally play an insignificant role, being only important for very low values of the relevant index ($\ll 100$). The *Kp* index is well fitted by a second-order power law function. The nonlinear relationship to *Kp* is partially understood upon realizing that *Kp* is a planetary index taken from 11 magnetometers in the geomagnetic latitude range −43.8°–62.5° [*Mayaud*, 1980] and hence is only partly influenced by the auroral electrojets. Nevertheless, we have included it simply because the index is readily available soon after the measurements. We have found that little is to be gained by using higher order polynomial fits to any of the indices.

AE and *Kp* are both measures of the magnetic disturbance on the ground. While *AE* is proportional to the magnitude of the disturbance, *Kp* is approximately proportional to the square root of the disturbance. Therefore it is self-consistent that we find Joule heating to be proportional to both *AE* and Kp^2. Given that $AE = AU - AL$ nT by definition, we can perform another internal consistency check by taking the equations for *AU* and *AL* from Table 1, computing $Q(j)$ as a function of $AU - AL$, and then comparing the result with

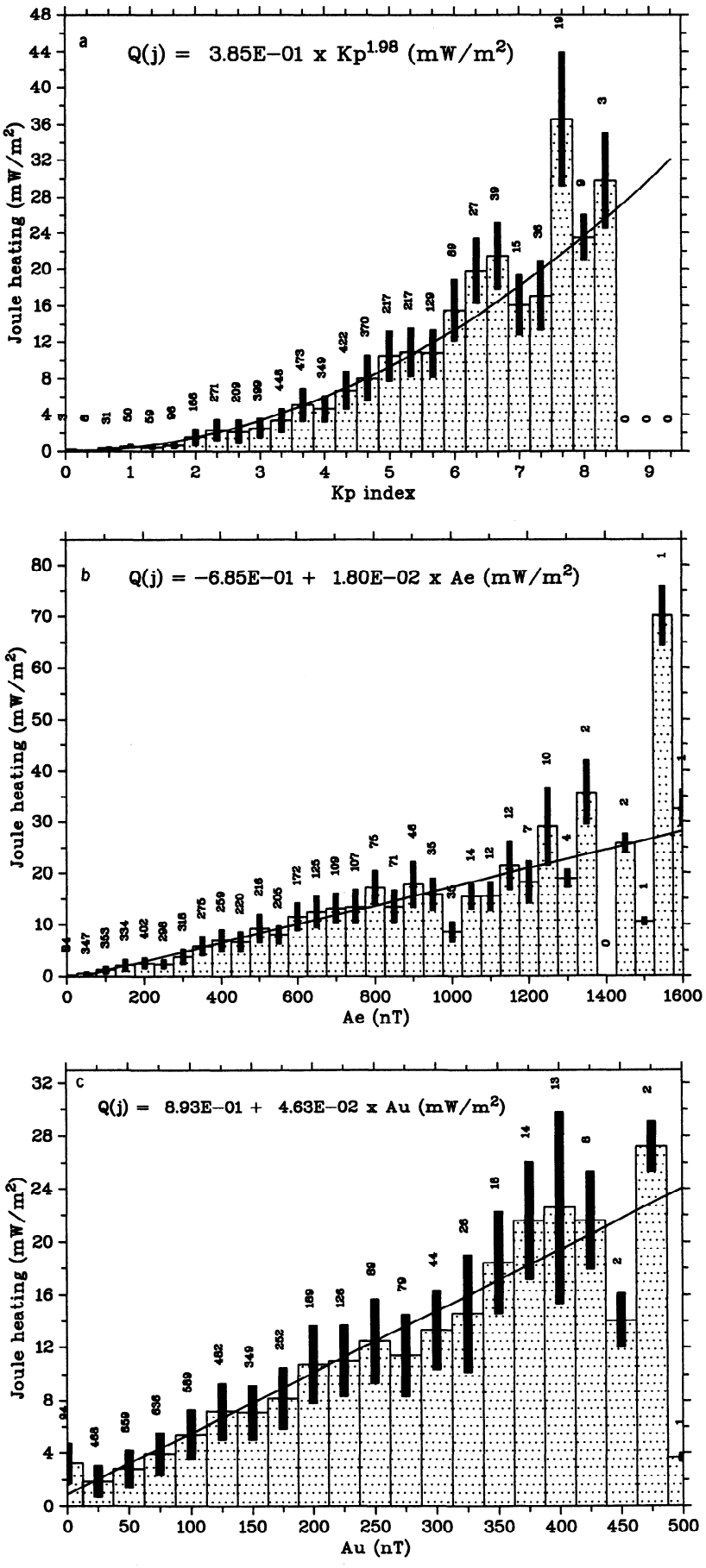

Figure 6. Average Joule heating as a function of the (a) Kp, (b) AE, (c) AU, and (d) AL indices.

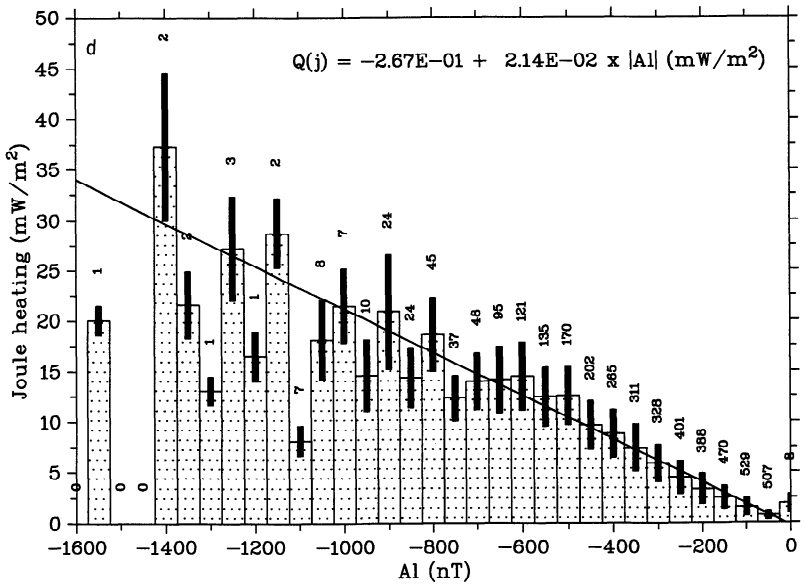

Figure 6. (continued)

the equation for AE from Table 1. Performing this procedure results in $Q(j) = -9.96 \times 10^{-5} + 1.46 \times 10^{-5} \times (AU - AL)$ W/m^2. The rate of increase of Joule heating with $AU - AL$ (1.46×10^{-5}) is very similar to that given in Table 1 for AE (1.8×10^{-5}). However, at first glance, the constant offset (-9.96×10^{-5}) appears to be somewhat different from that given in Table 1 (-6.85×10^{-4}). This apparent discrepancy is not serious, however, since the constant offsets are only significant for very low values of AE ($AE \ll 100$), where the uncertainties are increased anyway (see discussion for Figure 6).

Realizing that Joule heating is strongly time dependent (see Figure 5), we have also produced functional fits of averages for the westward and eastward electrojet regions only, in order to compare their relative contributions. To recap, for the westward (eastward) electrojet region, any equatorward (poleward) pointing electric field vector within ±45° of magnetic south (north) has been included in the data analysis. All other electric field vector directions are simply ignored. As was noted before, the radar systems receive no backscatter when the ionospheric electric field falls below the threshold (15 mV/m [*Cahill et al.*, 1978]), and hence there is no directional information for these data. For this analysis, these data are set to zero. As was seen earlier, this may result in an underestimate of up to 10%. However, we believe the error to be much smaller than this, since the radars generally receive most of their backscatter during these intervals, as indicated in Figure 4. The functional fits for the Kp, AE, AU, and AL indices are given for the westward and eastward electrojet regions in Tables 2 and 3, respectively.

The westward electrojet region produces higher levels of Joule heating than the eastward electrojet region, and this is consistent with the results shown in Figure 5 and Plate 1. In all cases, the rate of increase of Joule heating is greater for the westward than the eastward electrojet region. For the Kp index, it is interesting to note that the power law curve fit is greater than second order for both electrojet regions. The same comments given earlier concerning the prediction of negative Joule heating in some instances during very quiet periods apply here too. The same internal consistency check used for the equations of table 1 may be employed here ($AE = AU - AL$ nT), giving $Q(j) = 9.96 \times 10^{-5} + 9.57 \times 10^{-6} \times (AU - AL)$ and $Q(j) = 3.27 \times 10^{-4} + 6.29 \times 10^{-6} \times (AU - AL)$ W/m^2 for the westward and eastward electrojet regions, respectively. The comparison of these equations with those given in Tables 2 and 3 is very good, lending confidence to the computational procedure.

Using the Chatanika radar, *Vickrey et al.* [1982] found that for a given electrojet current intensity, more energy is deposited in the premidnight eastward than in the postmidnight westward electrojet sector. They also found the rate of increase of Joule heating with current intensity is larger for the eastward than for the westward electrojet. They explained this in terms of changing conductivity. In general, morning sector precipitation is harder, thereby enhancing the Hall-to-Pedersen conductivity ratio relative to the evening sector. Hence the westward electrojet region is less dissipative than the eastward electrojet region. A similar conclusion was reached by *Brekke and Rino* [1978]. How-

Table 1. Functional Fits of Average Joule Heating for All the Data for the Kp, AE, AU, and AL Indices

Index	Fit
Kp	$Q(j) = 3.85 \times 10^{-4} \times Kp^{1.98}$ W/m^2
AE	$Q(j) = -6.85 \times 10^{-4} + 1.80 \times 10^{-5} \times AE$ W/m^2
AU	$Q(j) = 8.93 \times 10^{-4} + 4.63 \times 10^{-5} \times AU$ W/m^2
AL	$Q(j) = -2.67 \times 10^{-4} + 2.14 \times 10^{-5} \times \|AL\|$ W/m^2

Table 2. Functional Fits of Average Joule Heating for the Westward Electrojet Region for the Kp, AE, AU, and AL Indices

Index	Fit
Kp	$Q(j) = 8.94 \times 10^{-5} \times Kp^{2.65}$ W/m^2
AE	$Q(j) = -7.68 \times 10^{-4} + 1.25 \times 10^{-5} \times AE$ W/m^2
AU	$Q(j) = 7.67 \times 10^{-4} + 2.88 \times 10^{-5} \times AU$ W/m^2
AL	$Q(j) = -2.32 \times 10^{-4} + 1.43 \times 10^{-5} \times \|AL\|$ W/m^2

Table 3. Functional Fits of Average Joule Heating for the Eastward Electrojet Region for the *Kp*, *AE*, *AU*, and *AL* Indices

Index	Fit
Kp	$Q(j) = 5.67 \times 10^{-5} \times Kp^{2.46}$ W/m^2
AE	$Q(j) = -7.15 \times 10^{-4} + 8.02 \times 10^{-6} \times AE$ W/m^2
AU	$Q(j) = 1.47 \times 10^{-4} + 1.90 \times 10^{-5} \times AU$ W/m^2
AL	$Q(j) = 5.62 \times 10^{-4} + 9.41 \times 10^{-6} \times \lvert AL \rvert$ W/m^2

ever, these observations contradict our findings given in Tables 2 and 3. It is interesting to note that Plate 2, where a constant uniform conductivity of 5.85 mhos was employed in the Joule heating calculation, appears to agree with the findings of the other authors. This possibly indicates a problem in using static average models of conductivity, since the other authors had the advantage of direct radar measurements of conductivity.

Ahn et al. [1983] stated that the geomagnetic indices *AE* and, particularily, *AL* make good indicators of the global energy deposition rates. Other workers also have produced estimates of global Joule heating as a function of the *Kp*, *AE*, *AU*, or *AL* indices. Their results, along with ours, are listed in Table 4 for comparison. We can estimate the total hemispherical Joule heating from the average functions given in Table 1 simply by multiplying each of the equations by the total hemispherical area in the latitude range 60°–80° (3.03×10^{13} m^2), since this is the region where the majority of Joule heating takes place [*Ahn et al.*, 1983].

For the *Kp* index, *Foster et al.* [1983] found that total hemispherical Joule heat input at the equinoxes varied linearly with *Kp* in the range $0 < Kp < 6$. We cannot agree with this result. Figure 6a clearly demonstrates that a linear function would make a poor fit. For the *AE*, *AU*, and *AL* indices, our results agree reasonably well with those of other authors (see Table 4). However, we tend to overestimate the rate of increase of total hemispherical Joule heating with increasing index value. The only exception is that of *Akasofu* [1979] (*AE* index), whose estimate is greater than ours. Some possible reasons for this discrepancy are now given. It was stated earlier that most of the Joule heat dissipation occurs within the zone bounded by 60° and 80° geomagnetic latitude [*Ahn et al.*, 1983], with the strongest heating tending to occur near 70° [*Banks et al.*, 1981]. This formed the basis of our extrapolation, and this assumption may not be entirely correct. Both *Schlegel* [1988] and *Ahn et al.* [1989] have found that *Spiro et al.*'s [1982] model generally overestimated ionospheric conductivity. Such a systematic error would linearly boost our Joule heating estimates. Joule heating estimates are relatively sensitive to the electric field measurement, since they are proportional to the square of electric field. It is possible that the empirically corrected STARE and SABRE radar electric field estimates [*Nielsen and Schlegel*, 1983, 1985] have a systematic error, as the correction algorithm is based on a relatively small data set (38 hours), which was biased toward the eastward electrojet. It is probable that a combination of the above is the reason for our apparent overestimation of total hemispherical Joule heating.

The average Joule heating within the radars' combined field of view has been determined as a function of the interplanetary magnetic field (IMF) B_x, B_y, and B_z components for the entire data set. Figure 7 shows the results as bar graphs, where Figures 7a, 7b, and 7c correspond to the B_x, B_y, and B_z components, respectively. In all cases, the data have been binned into steps of 1 nT. For each bin, twice the standard deviation on the mean is plotted as a solid bar. The number of hours of data contributing to each average, rounded to the nearest hour, is given above each bin. Only a fraction of the available Joule heating data contributed to the distributions of Figure 7, as there were many intervals for which no IMF data were available. In all cases, many of the data occur for small IMF amplitudes. There is a definite trend toward increased Joule heating for $B_z < 0$. This is not unexpected, as it has been generally long accepted that magnetospheric convection increases when $B_z < 0$ [cf. *Dungey*, 1961], thus producing greater ionospheric electric field strengths. It is possible to demonstrate this point simply by replacing *Spiro et al.*'s [1982] conductivity model with a constant uniform value. The function of Joule heating with B_z can then only be a result of electric field variations. This is shown for B_z in Figure 7d, where the conductivity has been set to 5.85 mhos (see discussion for Plate 2). Clearly, Figures 7c and 7d have a very similar functional form, demonstrating that ionospheric electric fields are indeed enhanced for $B_z < 0$. For B_y and B_x, there are no clear trends, although one might tentatively conclude that Joule heating is greater for either $B_y \gg 0$ or $B_x \ll 0$. The $B_x \ll$

Table 4. Functional Fits of Total Hemispherical Joule Heating

Index	Fit	Reference
Kp	$Q(j) = 1.17 \times 10^{10} \times Kp^{1.98}$ W	this paper
	$Q(j) = 4.0 \times 10^9 + 2.0 \times 10^{10} \times Kp$ W	*Foster et al.* [1983]
AE	$Q(j) = -2.08 \times 10^{10} + 5.45 \times 10^8 \times AE$ W	this paper
	$Q(j) = 8.00 \times 10^8 \times AE$ W	*Akasofu* [1979]
	$Q(j) = 1.00 \times 10^8 \times AE$ W	*Perreault and Akasofu* [1978]
		Akasofu and Kamide [1980]
	$Q(j) = 2.00 \times 10^8 \times AE$ W	*Akasofu* [1981]
	$Q(j) = 1.60 \times 10^{10} + 1.75 \times 10^8 \times AE$ W	*Spiro et al.* [1982]
	$Q(j) = 2.30 \times 10^8 \times AE$ W	*Ahn et al.* [1983]
	$Q(j) = 3.20 \times 10^8 \times AE$ W	*Baumjohann and Kamide* [1984]
AU	$Q(j) = 2.71 \times 10^{10} + 1.40 \times 10^9 \times AU$ W	this paper
	$Q(j) = 4.20 \times 10^8 \times AU$ W	*Baumjohann and Kamide* [1984]
AL	$Q(j) = -8.09 \times 10^9 + 6.48 \times 10^8 \times \lvert AL \rvert$ W	this paper
	$Q(j) = 3.00 \times 10^8 \times \lvert AL \rvert$ W	*Ahn et al.* [1983]
	$Q(j) = 2.50 \times 10^8 \times \lvert AL \rvert$ W	*Baumjohann and Kamide* [1984]

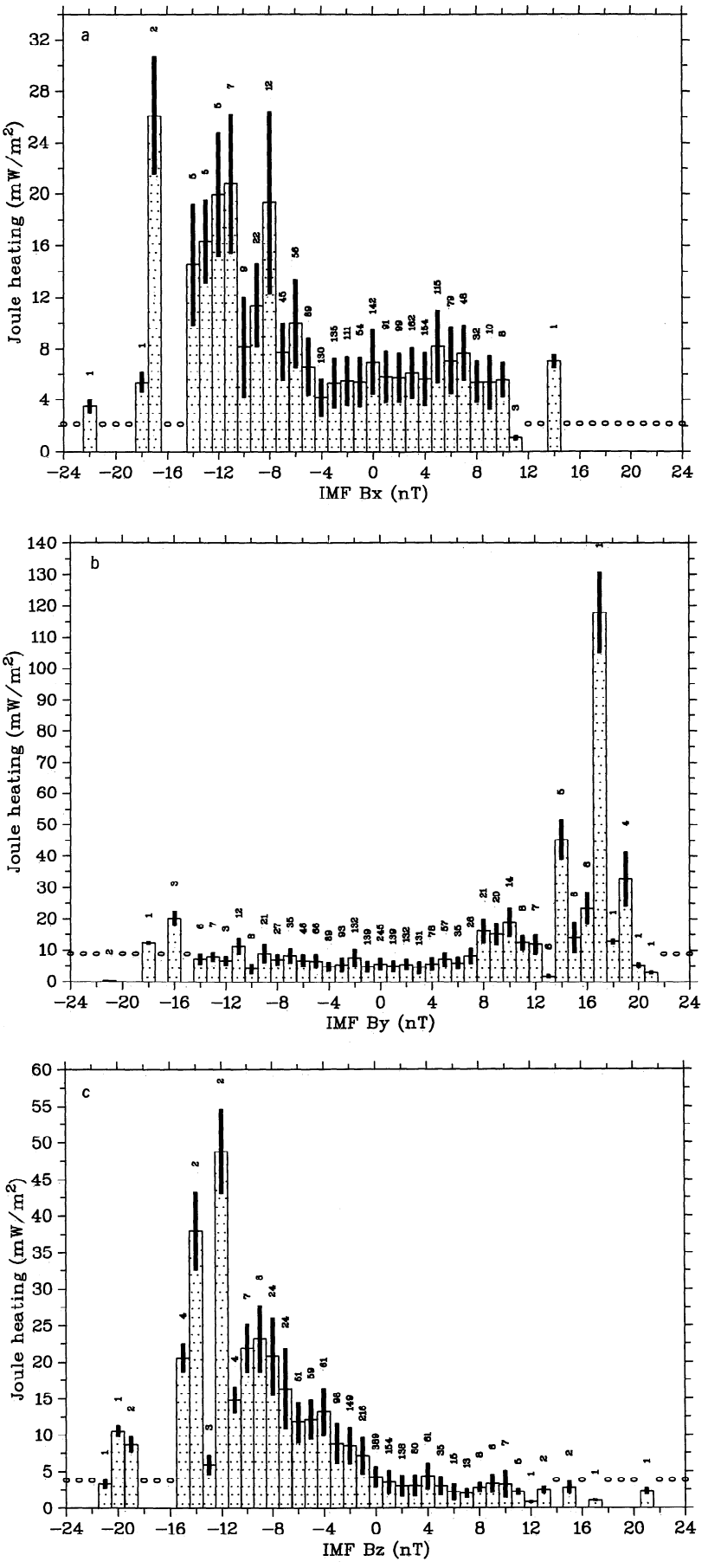

Figure 7. Average Joule heating, using *Spiro et al.*'s [1982] empirical conductivity model, as a function of the (a) B_x, (b) B_y, and (c) B_z components of the interplanetary magnetic field. Figure 7d shows the same result as Figure 7c, assuming a constant uniform conductivity distribution of 5.85 mhos.

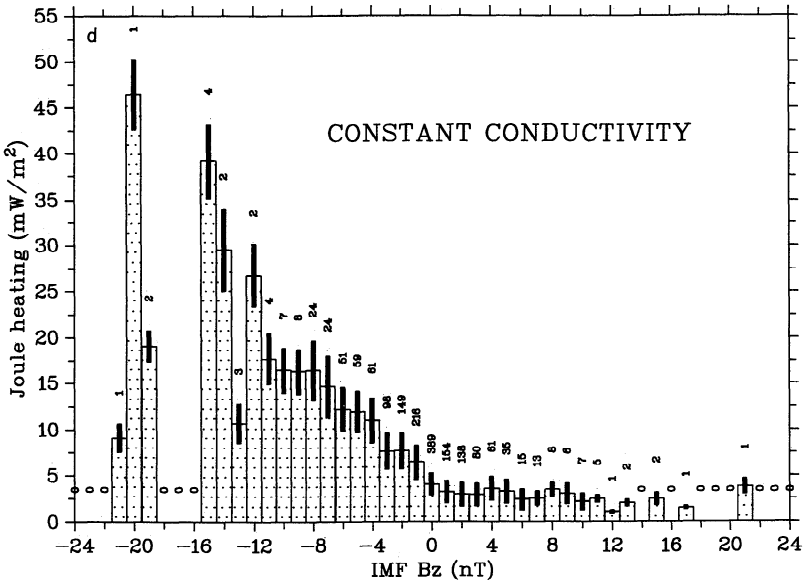

Figure 7. (continued)

0 is only slightly more convincing. Very few data contribute to the large-amplitude IMF values, and given that Joule heating is strongly time dependent (see Figure 5), the possible trends for B_y and B_x may be fictitious.

The importance of the IMF on substorm activity has been known for some time [cf. *Akasofu*, 1980, and references therein], especially the southward component. Among other things, a sudden southward turning of the IMF can lead to enhanced plasma convection and the occurrence of a substorm. Unfortunately, it is not possible to make real-time plots showing the interaction between Joule heating and IMF B_z simply because the electric field and B_z are derived from actual measurements, while conductivity, in our case, is obtained from a statistically averaged model. However, we can show the interaction between the ionospheric electric field and B_z, since Joule heating is proportional to the electric field squared. This is illustrated in Figure 8 using two examples. Both panels show the average hourly electric field squared as shaded bars for a single 24-hour period referring to the left-hand axis. The hourly average IMF B_z amplitude is plotted as a heavy solid line using the right-hand axis.

Figure 8 clearly demonstrates that electric field squared (E^2) is generally enhanced when B_z is negative, and vice versa. When B_z is persistently positive, E^2 remains relatively low, for example, after 1500 UT in Figure 8a and after 0300 UT in Figure 8b. The opposite also appears to be true. While it is clear that the ionospheric electric field responds to changes in B_z and is probably the dominant component in Joule heating (see Figure 7d), there are obviously other important factors. This is well demonstrated by the fact that the E^2 does not always react directly to B_z, for example, at 1900 UT in Figure 8a, where E^2 hardly increases at all when B_z suddenly goes negative, or after 1100 UT in Figure 8b, where E^2 increases without B_z going negative. One such factor is particle precipitation, causing substantial local modulations in conductivity. Since Joule heating is linearly dependent on conductivity, it is easily conceivable that local variations in conductivity could temporarily dominate the electric field contribution to Joule heating.

The response time of the magnetosphere to the IMF B_z component has been studied using cross-correlation analysis between the AE index and B_z. *Rostoker et al.* [1972] and *Meng et al.* [1973] have found that AE lags B_z by 30–50 and 40 min, respectively. In our data, E^2 appears to respond to sign changes of B_z with a delay of about an hour. This agrees well with the other authors to within our relatively poor time resolution of only 1 hour.

Conclusion

Ionospheric electric field estimates from two bistatic coherent radar systems, STARE and SABRE, combined with a static ionospheric conductivity model, have been used to produce an estimate of average ionospheric Joule heating with good spatial and temporal resolution over 8.8° of latitude. The electrojet regions are the main contributors, with the postmidnight westward electrojet region dissipating more energy over a greater area than the premidnight eastward electrojet region. Average Joule heating appears to be linearly related to the AE, AU, and AL indices, whereas for the Kp index a quadratic power law gives the best relationship. Generally, there is a distinct increase in electric field strength when the IMF B_z component is negative, i.e., pointing southward. The ionospheric electric field appears to respond to changes in sign of B_z with a delay of about an hour.

It is unwise to use global statistically averaged conductivity models for the study of single events, as they can only give a crude approximation to reality, yet knowing the instantaneous conductivity distribution is so important for a variety of studies. It has been demonstrated that the ionospheric conductivity may be inferred directly from, or with the assistance of, satellite auroral images [*Lummerzheim et al.*, 1991; *Robinson et al.*, 1989; *Kamide et al.*, 1986]. There now appears to be some evidence that it may be possible to extrapolate the height-integrated conductivities obtained from incoherent radars such as EISCAT to other regions of the local sky using simultaneous all-spectrum auroral images

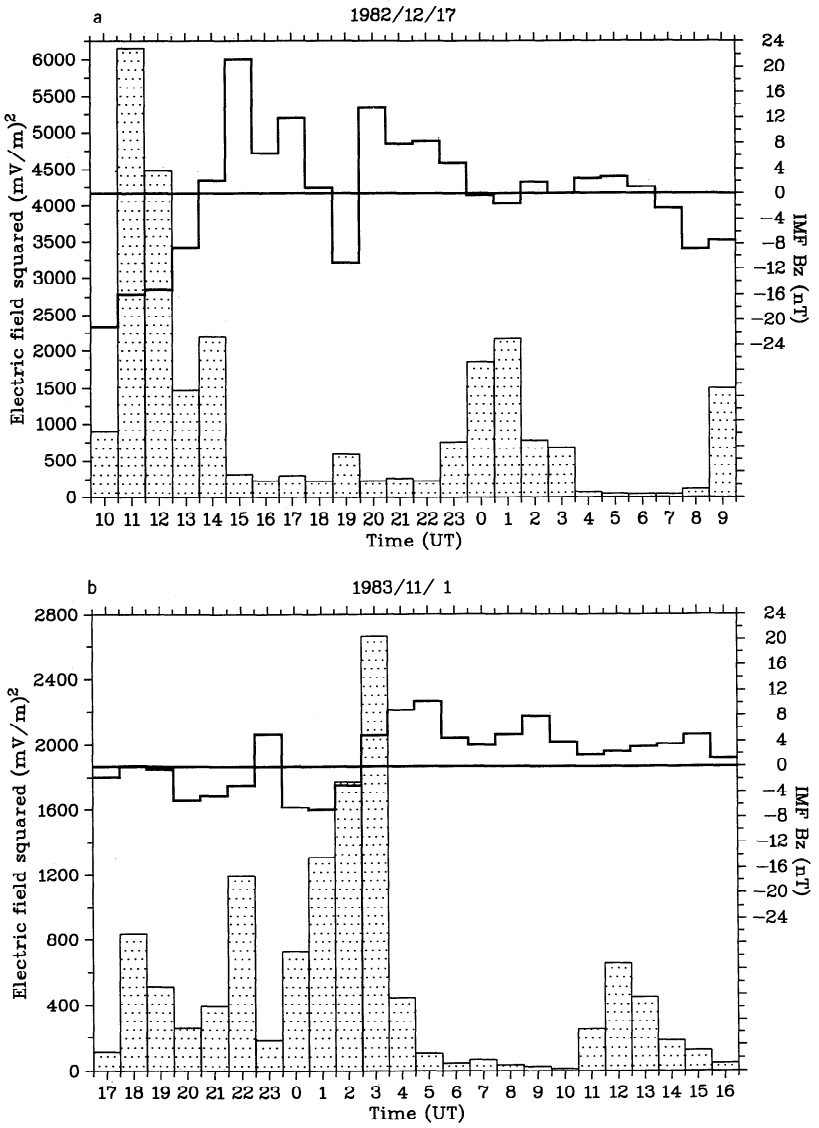

Figure 8. Average hourly electric field squared (shaded bars) and IMF B_z component (solid line) for a 24-hour period starting at (a) December 17, 1982, 1000 UT and (b) November 1, 1983, 1700 UT.

[*Kaila et al.*, 1993]. We intend to test this possibility using an all-sky TV system newly installed near the center of the STARE field of view. If this comes to fruition, then it will become possible to use the STARE and EISCAT radars to estimate instantaneous Joule heating rates over the large area covered by the STARE radar with very high spatial and temporal resolution. This would be most useful, for example, in auroral zone dynamics and substorm studies.

Acknowledgments. The STARE radars were operated by the Max Planck Institut für Aeronomie (Germany) in cooperation with ELAB, the Norwegian Technical University (Trondheim), and the Finnish Meteorological Institute (Helsinki). The SABRE radars were operated jointly by the Max Planck Institut für Aeronomie (Germany) and by the Leicester University (United Kingdom) in cooperation with the Uppsala Ionospheric Observatory (Sweden). The authors wish to thank the World Data Center C2 for Geomagnetism, Kyoto University (Japan), for supplying the *AE* data electronically.

The Editor thanks Asgeir Brekke and Raymond A. Greenwald for their assistance in evaluating this paper.

References

Ahn, B.-H., S.-I. Akasofu, and Y. Kamide, The Joule heat production rate and the particle energy injection rate as a function of the geomagnetic indices *AE* and *AL*, *J. Geophys. Res.*, *88*, 6275–6287, 1983.

Ahn, B.-H., H. W. Kroehl, Y. Kamide, and D. J. Gorney, Estimation of ionospheric electrodynamic parameters using ionospheric conductance deduced from Bremsstrahlung X ray image data, *J. Geophys. Res.*, *94*, 2565–2586, 1989.

Akasofu, S.-I., Relationship between the growth of the ring current and the interplanetary quantity η, *Planet. Space Sci.*, *27*, 1039–1041, 1979.

Akasofu, S.-I., The solar wind–magnetosphere energy coupling and magnetosphere disturbances, *Planet. Space Sci.*, *28*, 495–509, 1980.

Akasofu, S.-I., Energy coupling between the solar wind and the magnetosphere, *Space Sci. Rev.*, *28*, 121–190, 1981.

Akasofu, S.-I., and Y. Kamide, Recent progress in studies of magnetospheric storms and substorms, *J. Geomagn. Geoelectr.*, *32*, 585–615, 1980.

Akasofu, S.-I., B.-H. Ahn, Y. Kamide, and J. H. Allen, A note on the accuracy of the auroral electrojet indices, *J. Geophys. Res.*, *88*, 5769–5772, 1983.

Banks, P. M., Observations of Joule and particle heating in the auroral zone, *J. Atmos. Terr. Phys.*, *39*, 179–193, 1977.

Banks, P. M., J. C. Foster, and J. R. Doupnik, Chatanika radar observations relating to the latitudinal and local time variations of Joule heating, *J. Geophys. Res.*, *86*, 6869–6878, 1981.

Baumjohann, W., and Y. Kamide, Hemispherical Joule heating and the *AE* indices, *J. Geophys. Res.*, *89*, 383–388, 1984.

Brekke, A., Electric fields, Joule, and particle heating in the high-latitude thermosphere, *J. Atmos. Terr. Phys.*, *38*, 887–895, 1976.

Brekke, A., and C. L. Rino, High-resolution altitude profiles of the auroral zone energy dissipation due to ionospheric currents, *J. Geophys. Res.*, *83*, 2517–2524, 1978.

Brekke, A., J. R. Doupnik, and P. M. Banks, A preliminary study of the neutral wind in the auroral *E* region, *J. Geophys. Res.*, *78*, 8235–8250, 1973.

Brekke, A., J. R. Doupnik, and P. M. Banks, Incoherent scatter measurements of *E* region conductivities and currents in the auroral zone, *J. Geophys. Res.*, *79*, 3773–3790, 1974.

Brekke, A., J. Moen, and C. Hall, Studies of the conductivities in the auroral zone ionosphere, *J. Geomagn. Geoelectr.*, *43*, 441–465, 1991.

Cahill, L. T., Jr., R. A. Greenwald, and E. Nielsen, Auroral radar and rocket double probe observations of the electric field across the Harang discontinuity, *Geophys. Res. Lett.*, *5*, 687–690, 1978.

Cole, K. D., Energy deposition in the thermosphere caused by the solar wind, *J. Atmos. Terr. Phys.*, *37*, 939–949, 1975.

Dungey, J. W., Interplanetary magnetic field and the auroral zones, *Phys. Rev. Lett.*, *6*, 47–48, 1961.

Evans, D. S., N. C. Maynard, J. Trøim, T. Jacobsen, and A. Egeland, Auroral vector electric field and particle comparisons, 2, Electrodynamics of an arc, *J. Geophys. Res.*, *82*, 2235–2249, 1977.

Fejer, B. G., and M. C. Kelley, Ionospheric irregularities, *Rev. Geophys.*, *18*, 401–454, 1980.

Foster, J. C., J.-P. St.-Maurice, and V. J. Abreu, Joule heating at high latitudes, *J. Geophys. Res.*, *88*, 4885–4896, 1983.

Greenwald, R. A., W. Weiss, E. Nielsen, and N. R. Thomson, STARE: A new radar auroral backscatter experiment in northern Scandinavia, *Radio Sci.*, *13*, 1021–1039, 1978.

Hardy, D. A., M. S. Gussenhoven, R. Raistrick, and W. J. McNeil, Statistical and functional representations of the pattern of auroral energy flux, number flux, and conductivity, *J. Geophys. Res.*, *92*, 12,275–12,294, 1987.

Harel, M., R. A. Wolf, R. W. Spiro, P. H. Reiff, C.-K. Chen, W. J. Burke, F. J. Rich, and M. Smiddy, Quantitative simulation of a magnetospheric substorm, 2, Comparisons with observations, *J. Geophys. Res.*, *86*, 2242–2260, 1981.

Heppner, J. P., and M. L. Miller, Thermospheric winds at high latitudes from chemical release observations, *J. Geophys. Res.*, *87*, 1633–1647, 1982.

Kaila, K. U., R. Rasinkangas, and J. Kangas, Photometric calibration of auroral TV pictures during a pulsating patch event, *Ann. Geophys.*, *11*, 790–796, 1993.

Kamide, Y., and S.-I. Akasofu, Notes on the auroral electrojet indices, *Rev. Geophys.*, *21*, 1647–1656, 1983.

Kamide, Y., J. D. Craven, L. A. Frank, B.-H. Ahn, and S.-I. Akasofu, Modelling substorm current systems using conductivity distributions inferred from *DE* auroral images, *J. Geophys. Res.*, *91*, 11,235–11,256, 1986.

Killeen, T. L., Energetic and dynamics of the Earth's thermosphere, *Rev. Geophys.*, *25*, 433–454, 1987.

Kofman, W., and E. Nielsen, STARE and EISCAT measurements: Evidence for the limitation of STARE Doppler velocity observations by the ion acoustic velocity, *J. Geophys. Res.*, *95*, 19,131–19,135, 1990.

Lummerzheim, D., M. H. Rees, J. D. Craven, and L. A. Frank, Ionospheric conductances derived from DE-1 auroral images, *J. Atmos. Terr. Phys.*, *53*, 281–292, 1991.

Mayaud, P. N. (Ed.), *Derivation, Meaning, and Use of Geomagnetic Indices*, *Geophys. Monogr.*, vol. 22, p. 42, AGU, Washington, D. C., 1980.

Meng, C.-I., B. Tsurutani, K. Kawasaki, and S.-I. Akasofu, Cross-correlation analysis of the *AE* index and the interplanetary magnetic field B_z component, *J. Geophys. Res.*, *78*, 617–629, 1973.

Nielsen, E., Aspect angle dependence of mean Doppler velocities of 1-m auroral plasma waves, *J. Geophys. Res.*, *91*, 10,173–10,177, 1986.

Nielsen, E., and K. Schegel, A first comparison of STARE and EISCAT electron drift velocity measurements, *J. Geophys. Res.*, *88*, 5745–5750, 1983.

Nielsen, E., and K. Schlegel, Coherent radar Doppler measurements and their relationship to the ionospheric electron drift velocity, *J. Geophys. Res.*, *90*, 3498–3504, 1985.

Nielsen, E., W. Guttler, E. C. Thomas, C. P. Stewart, T. B. Jones, and A. Hedberg, A new radar auroral backscatter experiment, *Nature*, *304*, 712–714, 1983.

Perreault, P., and S.-I. Akasofu, A study of geomagnetic storms, *Geophys. J. R. Astron. Soc.*, *54*, 547–573, 1978.

Robinson, R. M., R. R. Vondrak, J. D. Craven, L. A. Frank, and K. Miller, A comparison of ionospheric conductances and auroral luminosities observed simultaneously with the Chatanika radar and the DE 1 auroral imagers, *J. Geophys. Res.*, *94*, 5382–5396, 1989.

Rostoker, G., H.-L. Lam, and W. D. Hume, Response time of the magnetosphere to the interplanetary electric field, *Can. J. Phys.*, *50*, 544–547, 1972.

Schlegel, K., Auroral zone E-region conductivities during solar minimum derived from EISCAT data, *Ann. Geophys.*, *6*, 129–138, 1988.

Spiro, R. W., P. H. Reiff, and L. J. Maher Jr., Precipitating electron energy flux and auroral zone conductance: An empirical model, *J. Geophys. Res.*, *87*, 8215–8227, 1982.

Theile, B., R. Boström, A. Dumbs, K. U. Grossmann, D. Krankowsky, P. Lämmerzahl, G. Marklund, E. Neske, G. Schmidtke, and K. Wilhelm, In situ measurements of heating parameters in the auroral ionosphere, *Planet. Space Sci.*, *29*, 455–468, 1981.

Vickrey, J. F., R. R. Vondrak, and S. J. Matthews, The diurnal and latitudinal variation of auroral zone ionospheric conductivity, *J. Geophys. Res.*, *86*, 65–75, 1981.

Vickrey, J. F., R. R. Vondrak, and S. J. Matthews, Energy deposition by precipitating particles and Joule dissipation in the auroral ionosphere, *J. Geophys. Res.*, *87*, 5184–5196, 1982.

Waldock, J. A., T. B. Jones, and E. Nielsen, Statistics of 1-m wavelength plasma irregularities and convection in the auroral *E* region, *Radio Sci.*, *20*, 709–717, 1985.

Wallis, D. D., and E. E. Budzinski, Empirical models of height integrated conductivities, *J. Geophys. Res.*, *86*, 125–137, 1981.

Wei, S., B.-H. Ahn, and S.-I. Akasofu, The global Joule heat production rate and the *Ae* index, *Planet. Space Sci.*, *33*, 279–281, 1985.

Wickwar, V., M. J. Baron, and R. D. Sears, Auroral energy input from magnetic electrons and Joule heating at Chatanika, *J. Geophys. Res.*, *80*, 4364–4367, 1975.

World Data Center C2 for Geomagnetism, *Data Book 22*, vol. 2, Kyoto University, Kyoto, Japan, 1993.

Zi, M., and E. Nielsen, Spatial variations of ionospheric electric fields at high latitudes on magnetic quiet days, *J. Geophys. Res.*, *87*, 5202–5206, 1982.

M. J. Kosch and E. Nielsen, Max-Planck-Institut für Aeronomie, Postfach 20, D-37189 Katlenburg-Lindau, Germany. (e-mail: nielsen@mirage.mpae.gwdg.de)

(Received April 14, 1994; revised March 3, 1995;
accepted March 3, 1995.)